Defence Research and Development Canada
Recherche et développement pour la défense Canada

DEFENCE R&D DÉFENSE

Effects of the instrument self-emission and source noise on long range infrared measurements of missile plumes

Simon Turbide
Tracy Smithson
Daniel St-Germain
DRDC Valcartier

Defence R&D Canada – Valcartier
Technical Report
DRDC Valcartier TR 2008-557
August 2009

Canada

Effects of the instrument self-emission and source noise on long range infrared measurements of missile plumes

Simon Turbide
Tracy Smithson
Daniel St-Germain
DRDC Valcartier

Defence R&D Canada – Valcartier

Technical Report
DRDC Valcartier TR 2008-557
August 2009

Principal Author

Simon Turbide, Ph. D.

Postdoctoral fellow

Approved by

Jean-Marc Garneau, Ph. D.

Section Head - Spectral and Geospatial Exploitation

Approved for release by

Christian Carrier

Chief Scientist - DRDC Valcartier

This work was conducted under Project Arrangement PA-CA-MDA-02-0001 between the US Missile Defense Agency and DRDC Valcartier.

Abstract

The DRDC Valcartier Spectral Imagery Laboratory currently supports hyperspectral imagers designed for field measurements. The ground-based Passive Infrared Ranging And Target Evaluation System (PIRATES) has been used over the years for the infrared signature characterization of different kinds of military related targets. This report highlights some issues observed in recent long range missile IR detection results, such as large negative features in the calibrated spectra. The bulk of these negative features are found to be related to instrument self-emission. Two algorithms are proposed to eliminate these features. The remaining negative peaks were the result of source instability, and appear principally in the peripheral region of the missile plume. Solutions are proposed to limit these negative features, such as tracking the missiles as smoothly as possible. The algorithms and solutions proposed will allow for the extraction of more accurate information from the original data.

Résumé

Le laboratoire d'imagerie spectrale de RDDC-Valcartier supporte présentement des imageurs hyperspectraux optimisés pour la mesure sur le terrain. Le capteur PIRATES a d'ailleurs été utilisé au fil des ans pour caractériser diverses cibles militaires à partir du sol. Ce rapport présente certaines anomalies observées dans les récentes mesures infrarouges de missiles à longue portée, notamment l'apparence de régions spectrales négatives. L'émission interne de l'instrument est responsable de la majorité des zones négatives. Deux algorithmes sont alors proposés pour éliminer ces effets indésirables. Les instabilités de source causent également l'apparence de raies négatives. Ces instabilités sont plus accentuées dans les régions périphériques du panache produit par les missiles. Des solutions sont proposées pour limiter l'impact de ces instabilités, dont la mise au point d'un système de poursuite aussi régulier que possible. Les algorithmes et solutions proposés dans ce rapport vont permettre une utilisation plus rigoureuse des mesures de missiles à longue portée, ainsi que de toute autre signature mesurée par le capteur.

This page intentionally left blank.

Executive summary

Effects of the instrument self-emission and source noise on long range infrared measurements of missile plumes

Turbide, S.; Smithson, T.; St-Germain, D.; DRDC Valcartier TR 2008-557; Defence R&D Canada – Valcartier; August 2009.

Introduction or background

The DRDC Valcartier Spectral Imagery Laboratory currently supports hyperspectral imagers designed for field measurements. The ground-based Passive Infrared Ranging And Target Evaluation System (PIRATES), and its portable version, Baby-PIRATES, have been used over the years for the infrared signature characterization of different kinds of military related targets. This report highlights some issues observed in recent long range missile measurements.

Results

The DELTA-4 missile infrared signature data set was collected in 2006 over a broad range of [60-400] km, with both PIRATES and Baby-PIRATES instruments. The standard calibration method was applied on the raw interferogram results, leading to large negative spectral regions in the missile calibrated spectra from PIRATES. No such features were observed with Baby-Pirates. A contributing factor to these distortions was discovered, it occurs when the instrument self-emission is hotter than the background and originates from the detector port of the instrument. To account for this effect, two alternative algorithms for calibration were proposed. It is shown that both methods remove the large negative regions from the data and produce results consistent with those from Baby-PIRATES.

There were also residual negative peaks observed with both instruments. These negative peaks were found to be due to source instability which could not be removed from the data with the two proposed algorithms. Spatially, these features appear in the peripheral region of the missile plume. It turns out that they have been caused mostly by the relative movement of the plume with the detector, rather than quick intensity variation within the plume. One should track the missile plume as smoothly as possible to limit the size of these negative peaks. Other parameters of the sensors, like the type of apodization, the spectral resolution, or the optical focus, also have an impact of the negative peaks.

Significance

The algorithms and solutions proposed here have been chosen for the generic calibration scheme to be used with the DRDC imaging spectrometer systems. This approach was found the most widely applicable method. The algorithms will allow for the extraction of more accurate information from the original long range missile data, as well as for all future measurements.

Future plans

This approach will be the method used for real-time calibration of DRDC spectral imagery measurement [1].

Sommaire

Effects of the instrument self-emission and source noise on long range infrared measurements of missile plumes

Turbide, S.; Smithson, T.; St-Germain, D.; DRDC Valcartier TR 2008-557; R & D pour la défense Canada – Valcartier; Août 2009.

Introduction ou contexte

Le laboratoire d'imagerie spectrale de RDDC Valcartier supporte présentement des imageurs hyperspectraux optimisés pour la mesure sur le terrain. Le capteur PIRATES, ainsi que sa version portable, Baby-PIRATES, ont d'ailleurs été utilisés au fil des ans pour caractériser diverses cibles militaires à partir du sol. Ce rapport présente certaines anomalies observées dans les récentes mesures de missiles à longue portée.

Résultats

Les signatures infrarouges du missile DELTA-4 ont été recueillies en 2006, sur des bandes de distances de [60-400] km, avec PIRATES et Baby-PIRATES. La méthode conventionnelle d'étalonnage a été appliquée sur les interférogrammes bruts, et de larges bandes de fréquences négatives ont été observées dans les spectres étalonnés du missile mesurés par PIRATES. Puisque de telles anomalies ne sont pas observées dans les résultats de Baby-PIRATES, il en découle qu'un comportement de l'instrument doit en être la cause. Cela se produit lorsque l'émission interne de l'instrument est plus intense que l'arrière-plan et provient du port du détecteur. Deux algorithmes alternatifs pour l'étalonnage sont donc proposés, chacun éliminant les régions négatives et produisant des résultats qui correspondent en conformité avec ceux de Baby-PIRATES. Toutefois, des raies spectrales négatives sont également observées avec PIRATES et Baby-PIRATES. Ces raies négatives résiduelles sont causées par les instabilités de source et ne peuvent être éliminées par les deux algorithmes mentionnés. Dans la dimension spatiale, ces raies négatives apparaissent principalement dans les zones périphériques du panache produit par le missile et elles sont causées par des déplacements relatifs entre le panache et le détecteur plutôt que par variations d'intensités rapides à l'intérieur du panache. La mise au point d'un système de poursuite plus régulier est suggérée afin de limiter l'importance des raies spectrales négatives. D'autres paramètres peuvent également affecter ces raies négatives, comme le choix d'apodization, la résolution spectrale ou le focus optique.

Importance

Les algorithmes et solutions proposés dans ce rapport ont été sélectionnés afin que la méthode d'étalonnage soit la plus largement applicable aux spectromètres imageurs de DRDC. Cette méthode d'étalonnage va permettre une utilisation plus rigoureuse des mesures de missiles à longue portée ainsi que des diverses autres mesures qui seront prises dans le futur.

Perspectives

La méthode proposée est celle qui sera utilisée pour le projet d'étalonnage en temps réel des mesures de spectromètres imageurs de DRDC [1].

Table of contents

List of figures

List of tables

Acknowledgements

We would like to thank Dr. Henry Buijs and Dr. Raphaël Desbiens for useful discussions.

This page intentionally left blank.

1 Introduction

The DRDC Valcartier Spectral Imagery Laboratory (SIL) is the focal point for Infrared (IR) Spectral Imagery measurements and research in IR multi- and hyper-spectral instrumentation and signal processing. Currently this laboratory supports two key Spectral Imagers (SI) designed for field measurements (AIRIS and PIRATES), and a third (BP) appropriate for both field and laboratory applications. The AIRIS instrument is designed for air-borne applications involving nadir measurements of ground targets (typically using a Convair 580 or DC-3 air platform). The PIRATES and BP instruments are designed for ground-based measurements, including tracking of moving targets such as aircraft. For moving target applications the SI instruments are mounted on the SIL Tracking Pedestal (SITP). The three SI instruments can also be operated from the SIL mobile laboratory (SIML); a climate controlled vehicle that can tow the SILTP. The SIML together with the SITP are Hercules C130 and C17 transportable.

All of the SI instruments use interferometry to provide the spectral and temporal resolutions of the SI data and use 8x8 element detector arrays to supply the spatial resolution. These systems can cover a very large IR region, capable of generating data spanning from 2 to 12 microns (830 to 5000 cm^{-1}). Spectral resolutions are also significant and can be varied from a maximum of 1 to a minimum of 16 cm^{-1}. Temporal resolutions are also high for this type of instrumentation spanning 4 to 50 Hz, depending on the spectral resolution. Sensitivity and area coverage are varied through the use of a number of different telescopes and output optic modules. For example AIRIS can operate with either a 3x or 9x telescope with IFOV's of 3.6 and 1.2 mrad, respectively. PIRATES can be operated with either a 2x or 22x telescope (5.5 or 0.5 mrad, respectively). The BP instrument is the most flexible, supporting 1x, 3x and 9x configurations (10.8, 3.6 and 1.2 mrad, respectively). In addition, these fields of view can be reduced by a factor of 4 through a change of output optic modules.

These instruments have been used for ground-based IR SI signature measurements of a variety of target types ranging from: tethered rockets at 50 meters, military vehicles at 1 km, ships at 2 km, aircraft at 5 km, and large missile systems up to 250 km (100 km altitude). AIRIS has been used to measure a variety of ground targets from altitudes ranging from 0.5 km to 7 km. For flexibility and security these systems store the raw measured data on removable media. A variety of software tools have also been developed and range from in-field quick-look inspection of the raw data to combine calibrated SI and imagery information. Although our field of application is typically described as hyperspectral imagery, it is actually hyperspectral video, as a fast succession of images is obtained (snap-shot), rather than one image recorded during a long period of time. Since hyperspectral imagery produces very high data rates, limiting the detection to an 8x8 array reduces the data rates. These spectral imagers thus constitute an interrogating system rather than a surveillance system.

The purpose of this document is to review the algorithm aspect of the standard approach to processing the raw data, and to report recent developments correcting some of the problematic results that can occur. The different processing methods will be illustrated by measurements made on long-range missiles: the missile ATLAS-II (2004, with PIRATES) and the missile DELTA-4

(2006 with both PIRATES and BP). The results from the InSb detectors (1900 to 5000 cm^{-1}) will be used.

The current status of PIRATES, BP and AIRIS, as well as the future development, will be the subject of the Chapter 2. The standard approach to transform an interferogram (the raw result of these instruments) into a calibrated spectrum is outlined in Chapter 3. Particular spectra with negative features, obtained with the standard method, are displayed in Chapter 4. The new modifications to the standard approach, needed to correct those negative features, are discussed in Chapter 5. One of the primary conditions for the application of interferometry, is a constant source over time. However, the average intensity produced by the missile, or any explosion, varies by many orders of magnitude along the event. When the time scale of the source's fluctuations is comparable to the time of a single scan, source noise will manifest itself in the processed data. The effect of this source noise on missile launch data, as well as possible solutions to reduce this effect, will be discussed in Chapter 6. Finally, the Chapter 7 contains our summary and conclusions.

2 Performance of PIRATES and BP

2.1 Current status

The PIRATES and BP sensors instruments are used for a variety of ground-based IR signature measurements ranging from the detection of explosions (on the order of second) to the detection of missile plumes (several minutes), with time, spatial and spectral resolutions. While the scan velocity of these instruments is limited by the response of the detectors, the frame rate varies according to the spectral resolution. Since the spectral resolution is directly related to the number of sampled points in the interferogram, the frame rate decreases as the number of sample points increases. For reference, the frame rates are 4 and 50 Hz for the spectral resolutions 1 and 16 cm^{-1} respectively. These rates are adjusted accordingly to the kind of target. In addition, the time of a scan must always be much smaller than the duration of the event under consideration. This criterion is important in order to reduce the variation of the source within a scan, and thus reduce as much as possible the source noise, as discussed in Chapter 6. Since 2004, the Pirates systems can follow the time evolution of target for as long as four hours, compared with the previous capability of 16 seconds.

The spatial resolution in these instruments is related to the number of pixels in the detector arrays. The limitation on the number of pixels stems from the amount of data to collect and process. In addition, high spectral resolution may be required in order to identify spectral features. Note also that, as discussed in the previous paragraph, the time and spectral resolutions are directly connected. The effect of the spectral resolution is shown in Figure 1. A section of a plume is plotted at 1 cm^{-1} and 4 cm^{-1}. The later spectrum is obtained by truncating the initial interferogram by a factor of 4. Degrading the resolution affects the shape of the spectrum; the height of the peaks decreases and their width increases. As shown in Figure 1, some closely spaced peaks at 1cm^{-1} appears as a continuum at 4 cm^{-1} resolution. While higher resolution is needed for spectroscopic studies, it will be seen in Chapter 6 that the source noise becomes more important as the resolution increases. Furthermore, in a missile launch, the power detected during the first instance originates mainly from the plume, while the emission is dominated by the nozzle for the later instance of the trajectory (the plume being too weak at that point to be seen). There are many orders of magnitude between the intensity coming from the early plume and the late nozzle emission. In these cases it becomes important to use a lower resolution during the last instance of the missile evolution (weak signal), in order to reduce the importance of noise coming from the instrument, since the noise information is mostly contains in the edge of an interferogram. It is thus really important to have an instrument allowing for the change of its spectral resolution quickly.

The PIRATE and BP sensors are thus flexible instruments that have been optimized for target identification by the Canadian Forces. Indeed, the spectral resolution (and so the scan speed) and the gain from the pre-amplificator can be changed on the fly to improve the detection efficiency. There is also a real-time feedback on the spectral data: the non-calibrated spectra and the integrated intensity of these non-calibrated spectra in each pixel, which gives an instantaneous picture of the source spatial disposition. Finally, for sources having time-scale variation much larger that the period of a scan, the signal can also be coadded to increase the signal-to-noise ratio, and thus generates clearer spectra.

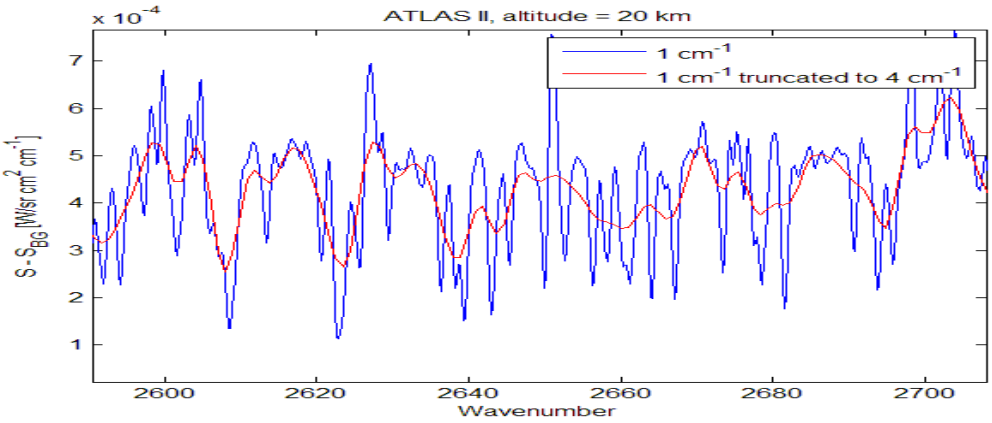

Figure 1: Effect of resolution on an ATLAS-II spectrum

2.2 Future developments

The hyperspectral imagery produces very high data rates. As an example, for a 4 cm^{-1} spectral resolution, the data rate is 32 MB/s. The data transfer from the data acquisition system to an external computer is currently done after the data collection, and thereafter, it takes weeks to calibrate all spectra. A real-time processing capability is now under work for AIRIS. The real time production of calibrated spectra, for each pixel, will make the data more directly exploitable, and will also reduce tremendously the post-experiment data processing time.

3 Description of the Standard Method Used to Process the Results

3.1 Numerical filtering and apodization

The raw data produced by the instrument is called an interferogram I_1. In our applications, the sources are usually not constant in time, which cause the interferograms to be highly asymmetric. The effects of source noise will be discussed later in Chapter 6. The first step toward improving the data is the application of a numerical filter, adjusted to cover the response band of the detectors. The effect of the numerical filtering is shown in Figure 2 and illustrates the reduction of the low frequency oscillations present in the original interferogram. The filter function F acts in the frequency space. From the properties of the Fourier Transform, the numerically filtered interferogram I_2 is simply given by the convolution of the original interferogram with the Fourier Transform of the filter : $I_2 = I_1 * FFT(F)$. Since the recorded interferograms are not continuous functions (sampled at discrete position), the Fourier Transform has to be replaced by the discrete Fourier Transform. The *FFT* notation refers to the Fast Fourier Transform algorithm 0, which is used to evaluate numerically the discrete Fourier Transform. The numerical filter now allows the application of an apodization function, on an almost symmetric interferogram. The interferogram I_2 is then multiplied by an apodizing function which removes false negative features in the transformed spectra because of the finite optical path displacement. The effect of apodization will be discussed later in Chapter 6.

At this point, we have an apodized double-sided interferogram including N sampled points $x=n\Delta x$, with n=[-N/2, -N/2+1,…, N/2-1]. The number of points N is adjusted to a power of 2 ($N=2^p$,) for the FFT algorithm to be more efficient. The zero path difference point (ZPD) is located at n=0. Interferograms are typically padded with zeros to double the length of the measured data. This results in a spectral description with 4 points per resolution element, ensuring photometric accuracy. The interferogram I, after zeropadding, contains 2N points. The uncalibrated complex target spectrum, at the index point $k=\sigma/\Delta\sigma$, is obtained from a discrete Fourier transform of the interferogram :

$$S_M[k] = \sum_{n=-N+1}^{N} I[n]\exp(-i\pi nk/N) = FFT(I). \quad (1)$$

The wavenumber spacing $\Delta\sigma$, and the sampling distance Δx, are connected by the relation $\Delta\sigma\Delta x=1/2N$.

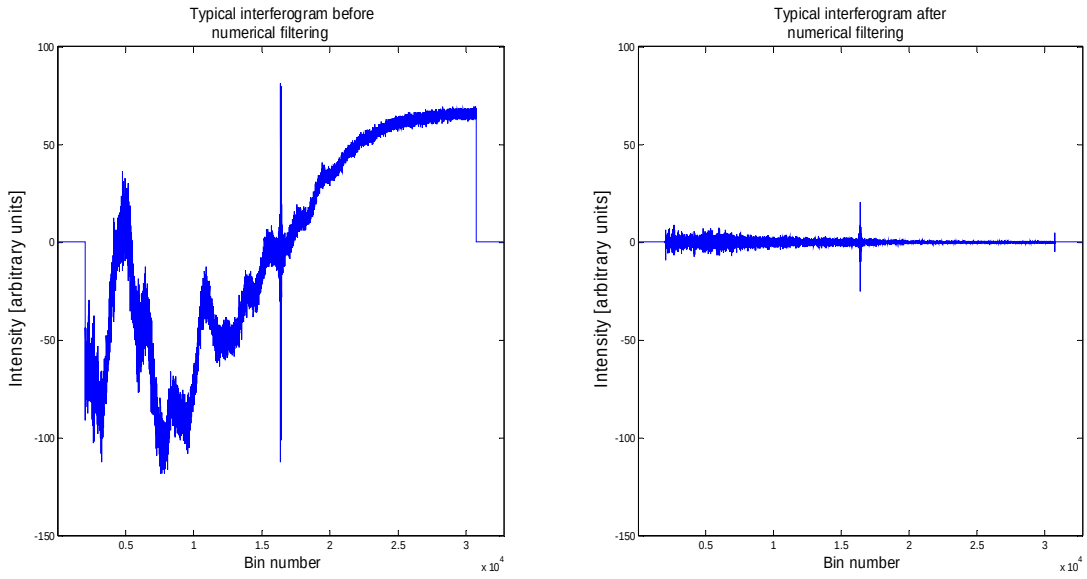

Figure 2: Effect of the numerical filter on a typical interferogram recorded during a missile launch

3.2 Phase correction

Any displacement of the ZPD point in the interferogram vector (i.e. ZPD point no longer located at n=0), or non-ideal behaviour of the beam-splitter and mirrors leads to a non-zero imaginary part in Eq.(1). The usual approach to extract the real spectrum is to apply a phase correction method in the first step, and then calibrate the resulting spectrum. The phase is removed using the Mertz [3][4] method. A double-sided low resolution interferogram I_3 is generated from the truncation of the full-resolution interferogram I, keeping M points around the ZPD. The interferogram I_3 is thereafter appodized and filled with ($2N$-M) zeros, in order to match the dimension of I. The phase is finally evaluated from this resulting interferogram I_4, according to

$$\phi[k] = \mathrm{Im}\left[\log\left(\frac{FFT(I_4)}{|FFT(I_4)|}\right)\right]. \tag{2}$$

The phase-corrected uncalibrated target spectrum is given by

$$S_{pc}[k] = \mathrm{Re}\left(S_M[k]e^{-i\phi[k]}\right) \tag{3}$$

3.3 Spectral calibration (Y-axis calibration)

The InSb photovoltaic detectors are characterized by the following linear relationship between the uncalibrated spectrum S_{pc} and the calibrated spectrum S:

$$S_{pc}[k] = R[k](S[k] + O[k]), \tag{4}$$

where the proportional factor R is the responsivity, and O is the offset resulting from instrument self-emission. In order to evaluate the instrument parameters in the 1900 to 5000 cm^{-1} band, two blackbodies (BB) with known temperatures and emissivities are used. To maximize the collection of light at high frequency (beyond 4000 cm^{-1}), a high temperature blackbody (T~400^{o}C) is necessary. However, to avoid saturation at lower frequencies, filters need to be applied. Two filters and four measurements are needed to find the instrument parameters (4-point method).

The four measurements needed are: ambient BB, hot BB with first filter, hot BB with second filter, hot BB with both filters. The corresponding phase-corrected spectra are respectively denoted by S_a, S^h_{f1}, S^h_{f2}, S^h_{f1f2}. The first filter is placed between the BB and the modulator, while the second filter is placed between the modulator and the detector, with a small angle to reduce channel spectrum effects. The self-emission of this filter directed toward the detector is not modulated: it will only add a DC offset and will not affect the transformed spectra. Its self-emissions directed toward the beam splitter, however, will be modulated by the interferometer and reflected back to the detector. This contribution is ignored, since there is no system of lenses or mirrors between this second filter and the beam splitter to collimate the beam. The self-emission of the first filter toward the beam-splitter will be collimated by the system of mirrors and modulated by the interferometer and must be taken into account.

The four measurements described above can be written by (dropping the [k] notation)

$$\begin{aligned} S_a &= R(B_a + O) \\ S_h^{f_1} &= R(f_1 B_h + E_{f_1} + O) \\ S_h^{f_2} &= R(f_2 B_h + O) \\ S_h^{f_1 f_2} &= R\left(f_2(f_1 B_h + E_{f_1}) + O\right) \end{aligned} \tag{5}$$

The left hand sides of Eq. (5) represent the phase corrected uncalibrated signals. The radiances of the hot (B_h) and ambient (B_a) blackbodies are given by

$$B_i = \varepsilon_i a_1 \sigma^3 \frac{1}{e^{a_2 \sigma / T_i} - 1}, \tag{6}$$

where a_1 = 1.19e-12 W/cm^2 sr cm^{-4} and a_2 =1.4388 cm K. The temperature and the emissivity of the blackbody are denoted respectively by T_i and ε_i. The transmittance of the filter i is denoted by f_i, while E_{f1} represents the first filter self-emission. The analytical expression of the responsivity (see Annex A for the details) is

$$R = \frac{-\left(\frac{B_a}{B_h}(X+Y)-Z\right)-\sqrt{\left(\frac{B_a}{B_h}(X+Y)-Z\right)^2-4\frac{XY}{B_h}\left(\frac{B_a}{B_h}(B_a-B_h)\right)}}{2\left(\frac{B_a}{B_h}(B_a-B_h)\right)} \tag{7}$$

where

$$\begin{aligned} X &= S_h{}^{f_1} - S_a \\ Y &= S_h{}^{f_2} - S_a \\ Z &= S_h{}^{f_1 f_2} - S_a \end{aligned} \tag{8}$$

The instrument offset is simply

$$O = \frac{S_a}{R} - B_a \tag{9}$$

The strong CO_2 and H_2O absorption within the instrument can cause the responsonsivity R to be very close to zero, which introduces large fluctuations in the calibrated spectrum proportional to $1/R$. To avoid these large fluctuations, the instrument's responsivity and offset are (linearly) interpolated in those regions. The calibrated results can then be interpreted by the signals incident of the detector, rather that the signals incident on the telescope, since the effect of the column of air inside the instrument is not removed. The absorption regions in which the interpolations are made are defined in Annex A. Finally, the calibrated target spectrum is given by

$$S = \frac{S_{pc}}{R} - O \tag{10}$$

Where S_{pc} is defined in Eq.(3). The units of S are W/sr cm^2 cm^{-1}. The calibration is done pixel by pixel, i.e. the responsivity and offset are evaluated for each pixel, and thereafter applied on a uncalibrated spectrum of the corresponding pixel. This is done to correct for vigneting effects that result in a loss of intensity as we move away from the optical axis. Vigneting is caused by the finite size of the optical system (lenses and mirrors), a mismatch between input and output optic focal lengths.

3.4 Frequency shift (X-axis calibration)

Due to the disposition of the mirrors, the light entering the modulator parallel to the optical axis will produces a spot at the center of the detector array. In order to produce an image, an incident beam with a finite extension must be collected. A given detector will collect the incident light on the modulator, providing that the light makes an angle with the optical axis, so that $\theta_{min} < \theta < \theta_{max}$. Due to geometrical considerations [5], a peak expected to be centered at the wavenumber σ_0 will be observed at σ_0 $(\cos(\theta_{min})+\cos(\theta_{max}))/2$. While the peak at σ_0 appears to be shifted by $\sigma_0(1-(\cos(\theta_{min})+\cos(\theta_{max}))/2)$, it is the whole X-axis that is compressed by the factor $(\cos(\theta_{min})+\cos(\theta_{max}))/2$. Each pixel has a different frequency shift: these shifts will increase as the pixels are displaced from the optical axis. The shift magnitude is evaluated, separately for each pixel, by measuring in a first instance the position of the H_2O absorption line expected to be located around 1868 cm^{-1} (in fact there is a group of lines around this position, but they resemble one peak at the measured 4 cm^{-1} resolution: the resolution at which the frequency shifts are evaluated). These positions are denoted by σ_x. Since the shifts are always directed toward the lower wavenumber, the pixel having the highest σ_x becomes the reference, i.e. the closest pixel to the optical axis. That referential position is denoted by σ_{ref} . The X-axis of each pixel is then calibrated by stretching each point of the vector σ by the factor σ_{ref} / σ_x :

$$\sigma' = \sigma \frac{\sigma_{ref}}{\sigma_x} \tag{11}$$

The X and Y axis calibrated spectrum is thus given by $S(\sigma'[k])$, where k is the index number. At this point, all pixels have been stretched by a different factor, so that their wavenumber vector σ' are all different. The spectra for each pixel are finally mapped onto a common wavenumber vector σ, by the interpolation of $S(\sigma')$.

In this section, the different steps of the standard method, to generate a calibrated spectrum from a raw interferogram, have been presented. The most critical step of this method is the phase correction. We will thus, in the following chapters, sometimes refer to the Mertz approach to design the standard method, since it is based on the Mertz method for the phase correction.

4 Results and Potential Problems with the Standard Method

We show in this chapter some results obtained for the DELTA-4 missile, using a Mertz approach, i.e. phase correction (Mertz method) followed by calibration. The results are shown for 1 cm^{-1} and 4 cm^{-1} resolution with the number of sampled points *N* in the interferograms, respectively 32768 and 8192. Figure 3 shows how the number of points *M* in the low resolution interferogram can affect a calibrated spectrum. The calibrated background has been subtracted from the target spectrum in this plot. The spectrum shows zero emission (within the noise level) in the CO2 absorption band [2200-2400] cm^{-1}, as it should, only when the high number of points is used (*M*=4096, corresponding to ~ 10% of *N*). However, for the case where *M*=128, a negative spectrum is obtained in this region. This *M*-dependency can be explained by looking at the target and background phases, as shown in Figure 4 (the phases are given by Eq.(2)). The background in the [1900-2500] cm^{-1} region has a smooth phase which is well described with both *M*=128 and *M*=4096. The plume, unlike the background, undergoes larges phase-shifts (shifts of π) in the [1900-2400] cm^{-1} region. A phase-shift of π corresponds to a sign inversion in the spectrum. These strong variations in the plume's phase cannot be well described by the small number of points *M*, and phase errors (of π) are obtained, causing some regions of the spectrum to be negative, as seen in Figure 3 (blue line below the red line).

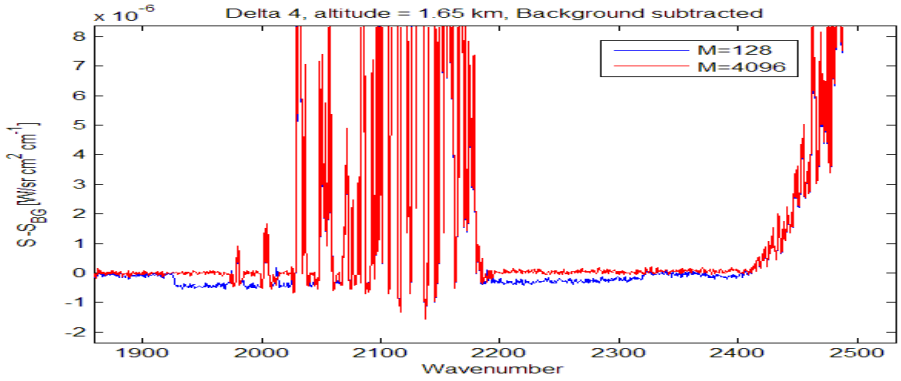

Figure 3: Portion of a plume spectrum (background subtracted) at 1 cm^{-1} resolution, as found by a Mertz method, for two differents values of M, where M is the number of points in the low resolution interferogram before zero filling. The altitude is 1.65 km and the range is 59 km.

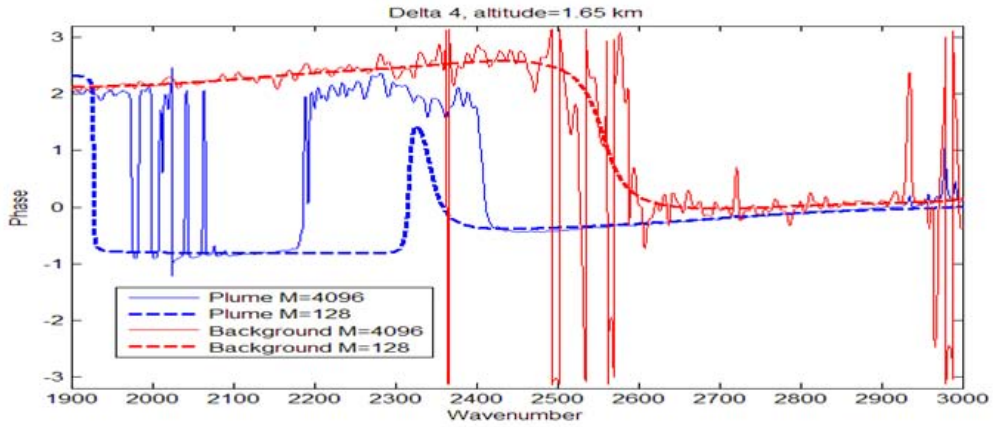

Figure 4: Phases extracted from the uncalibrated plume and background complex spectrum of Figure 3, using M = 128 and M=4096 points. The altitude is 1.65 km and the range is 59 km.

Large negative peaks have been observed in the DELTA-4 signature, measured at 1 cm^{-1} resolution, especially for the pixels located on the edges of the plume (see Chapter 6). An example is shown in Figure 5 for two values of *M* (left and right panels). Using a high value for *M* in this case, does not correct for these negative features, unlike the small negative regions observed in Figure 3, for small *M*.

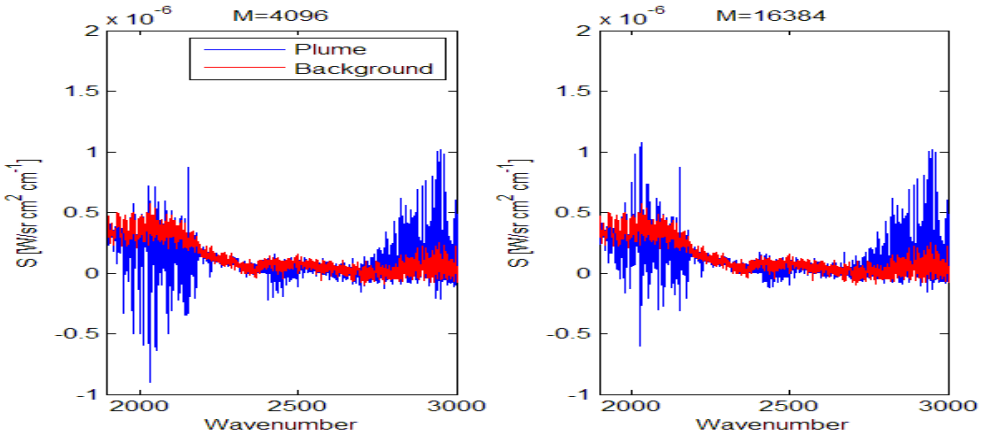

Figure 5: Calibrated plume and background spectra of DELTA-4 emissions at an altitude of 35 km and a range of 75 km, with 1cm^{-1} resolution. The number of points used for phase correction are M=4096 (left panel) and M=16384 (right panel).

Finally, as range and altitude increase, the target spectrum falls below that of the background by a significant amount (for σ < 2200 cm^{-1}), as seen in the left panel of Figure 6. For high altitudes (~ 100 km), the plume signature is so weak that only the nozzle can be detected. In these cases, a lower resolution is selected to reduce the level of noise. A naïve interpretation of the left panel of

Figure 6 would suggest that there is more energy in this region from the background than from the nozzle. We will see in the next chapter that this interpretation is not correct. The right panel in Figure 6 shows the phases extracted from the nozzle and the background measurements. Like the phases shown in Figure 4, some phase-shifts of π are again present. Here too, the nozzle spectrum could not be corrected (i.e. transformed to become larger than the background) by making *M* bigger. The spectra and phases, for both the nozzle and the background, obtained with the BP instrument, are shown in Figure 7. Here, altitude, range and resolution are the same than for Figure 6. The phases in Figure 7 are well behaved, without deep phase-shift, and the nozzle spectrum is always on top of the background spectrum, as it should be.

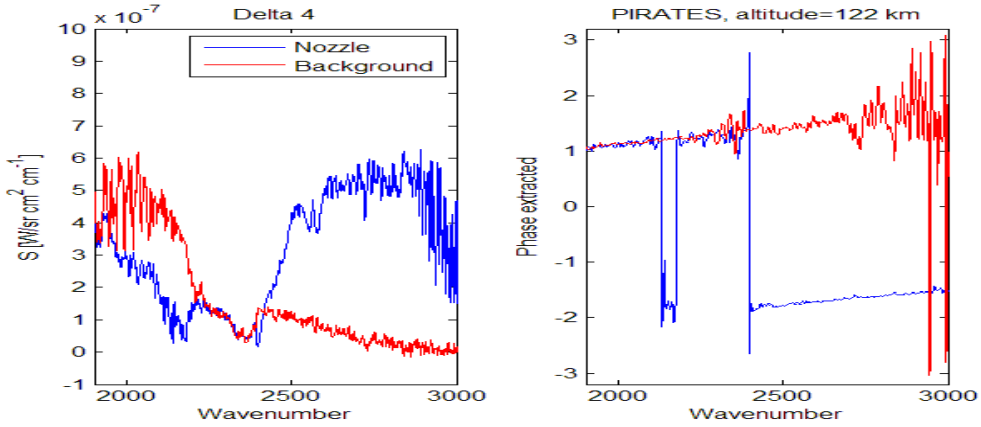

Figure 6: Calibrated Nozzle and Background spectra at 4cm^{-1} resolution, measured with PIRATES, for DELTA-4, at an altitude of 122 km and a range of 216 km. The right panel shows their phases as extracted with M=4096 points.

The results measured with the PIRATES and BP instruments are thus not fully consistent, as seen from Figure 6 and Figure 7. These inconsistencies in the DELTA-4 signal and phase measurements suggest an instrumental artifact. It will be discussed later in Chapter 5, that a possible cause might be a heater that was used to prevent condensation within PIRATES. It will also be discussed in Chapter 6 that the large negative peaks shown in Figure 5, and only seen at a 1 cm^{-1} resolution, are rather due to source noise. While these large negative peaks from Figure 5 are not instrumental artifacts, they are less pronounced in BP data because the higher resolution allowed by that instrument is 4 cm^{-1} (it is 1 cm^{-1} for PIRATES)

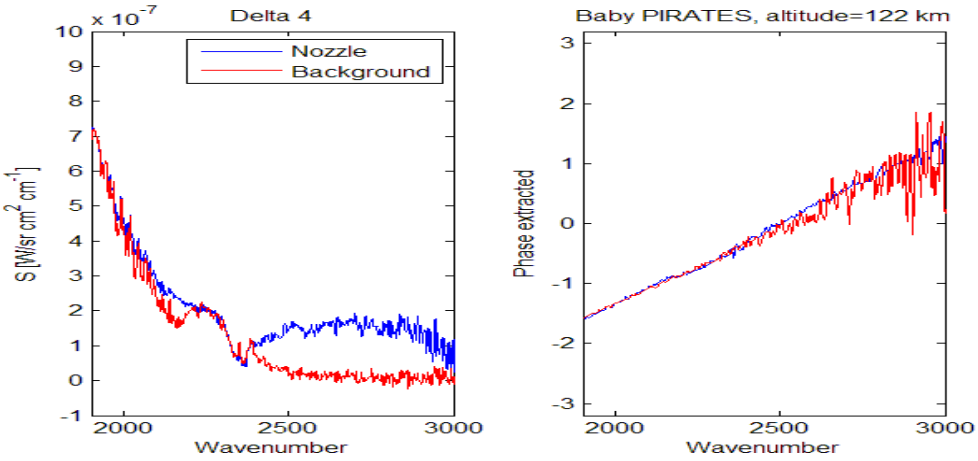

Figure 7: Idem Figure 6, but for the Baby PIRATES instrument

5 Alternative Methods to Correct the Problematic Results obtained with the Standard Method

5.1 Calibration using Complex Spectra

A solution to overcome the phase problems (instrumental artifacts) illustrated in the previous chapter has been developed by Revercomb *et al.*, in Ref.[6], for atmospheric sounding applications. In this approach, the instrument parameters are extracted directly from the uncalibrated complex spectra. These parameters are in turn applied to a complex target spectrum. A nice thing about this approach is that the extraction of a low resolution interferogram is not required, so there is no dependence on an arbitrary number of points *M*. However, this approach is only applicable on stable systems for which the phase does not fluctuate over time or between sets of measurements. In this approach, the uncalibrated complex BB spectra are given by

$$\begin{aligned}
\tilde{S}_a &= R(B_a + O_c)e^{i\phi};\\
\tilde{S}_h^{\,f_1} &= R(f_1 B_h + E_{f_1} + O_c)e^{i\phi};\\
\tilde{S}_h^{\,f_2} &= R(f_2 B_h + O_c)e^{i\phi};\\
\tilde{S}_h^{\,f_1 f_2} &= R\left(f_2(f_1 B_h + E_{f_1}) + O_c\right)e^{i\phi};
\end{aligned} \tag{12}$$

where the instrument offset O_c is complex. The set of equations above is similar to that from Eq. (5), at the difference that the spectra here are complex, because the phase ϕ has not yet been corrected for. The phase, which arises any time an interferogram is not symmetric, appears into an exponential form in the description of a complex spectrum, providing that the phase is a slowly varying function of the frequency [5]. It can be verified, from the figures of Chapter 4, that the phase varies slowly with the frequency.

The responsivity *R* is still given by Eq.(7), but with *X*, *Y* and *Z* now defined by

$$\begin{aligned}
X &= \mathrm{Re}\left[(\tilde{S}_h^{\,f_1} - \tilde{S}_a)e^{-i\phi}\right]\\
Y &= \mathrm{Re}\left[(\tilde{S}_h^{\,f_2} - \tilde{S}_a)e^{-i\phi}\right]\\
Z &= \mathrm{Re}\left[(\tilde{S}_h^{\,f_1 f_2} - \tilde{S}_a)e^{-i\phi}\right]
\end{aligned} \tag{13}$$

The phase is extracted from the relation

$$e^{i\phi} = \frac{\tilde{S}_h^{f_1} - \tilde{S}_a}{\left|\tilde{S}_h^{f_1} - \tilde{S}_a\right|} \tag{14}$$

The instrument offset is given by

$$O_c = \frac{\tilde{S}_a}{R} e^{-i\phi} - B_a \tag{15}$$

While the phases should be consistent between successive measurements sets, shifts up to 500 sampling points have been observed between the calibration (coadded measurements) ZPD and the target (single scan measurements) ZPD positions. This shift is the result of the data collect software. Assuming nothing more than a relative ZPD shift between the BB interferograms and the target interferogram, the uncalibrated complex target spectrum can be written as

$$S_M = R(S + O_c)e^{i\phi}e^{i\phi_{ZPD}} \tag{16}$$

We can write the relative phase as $\phi_{ZPD} = a\sigma + b$, where $b = \{0 \text{ or } \pi\}$: the $b = \pi$ is obtained when an overall negative sign appears between the coadded and single scan interferograms. From any single scan measurement including a high intensity targets, we obtain $S_M \approx RSe^{i\phi}e^{i\phi_{ZPD}}$, so that

$$\phi_{ZPD} \approx \mathrm{Im}\left[\ln\left(\frac{S_M e^{-i\phi}}{|S_M|}\right)\right]. \tag{17}$$

The parameters a and b can be evaluated from a linear fit of ϕ_{ZPD} vs σ. While the b parameter is fixed for all pixels, the slope a can change smoothly between pixels.

Since a high intensity target may not be available in each pixel (the navigation system is adjusted to align the plume with the center pixels), the a parameter must be evaluated generally, for each pixel, with no high-intensity target assumption. The calibrated target spectrum, within the complex calibration approach, from Eq. (16), will therefore be given by

$$S = \mathrm{Re}(Y), \tag{18}$$

with

$$Y = \frac{S_M}{R} e^{-i(\phi+\phi_{ZPD})} - O_c\,. \tag{19}$$

If the relative phase ϕ_{ZPD} is evaluated properly, the target signal would be included in the real part of *Y*, leaving only noise in the imaginary part of *Y*. Thus, the parameter *a* should minimize the imaginary part of *Y*. By the evaluation of $\Sigma_\sigma(\mathrm{Im}\ Y)^2$ as a function of *a*, a series of local maxima and minima are obtained, from which the lowest local minimum is found, a_0. For the second step in this procedure, Eq. (20)

$$\frac{\partial\left(\sum_\sigma (\mathrm{Im}\, Y)^2\right)}{\partial a} = 0 = \sum_\sigma \left(\mathrm{Im}\, Y\ \mathrm{Re}\left[\frac{S_M}{R} e^{-i(\phi + a\sigma + b)}\right]\sigma \right) \tag{20}$$

is solved numerically around $a = a_0$, and the relative phase $\phi_{ZPD} = a\sigma + b$ can be evaluated for each pixel. All frames can then be calibrated from Eq. (18).

The previous example spectra calibrated using the standard method, (shown in Figure 3, Figure 5 andFigure 6), have been calibrated with the complex method described in this chapter. The results are displayed in Figure 8, Figure 9 and Figure 10 (left panel). The negative features observed after background subtraction in the standard method have now been corrected. There are however some negative peaks, as shown in Figure 9, that have not been removed by the complex calibration method. The origin of these residual negative peaks will be discussed in Chapter 6. Then, the complex calibration method, unlike the standard method (Mertz), succeeds for the correction of most of the observed negative features. The complex method turns out to be equivalent to Mertz when the spectrum is already well behaved, as shown in the right panel of Figure 10.

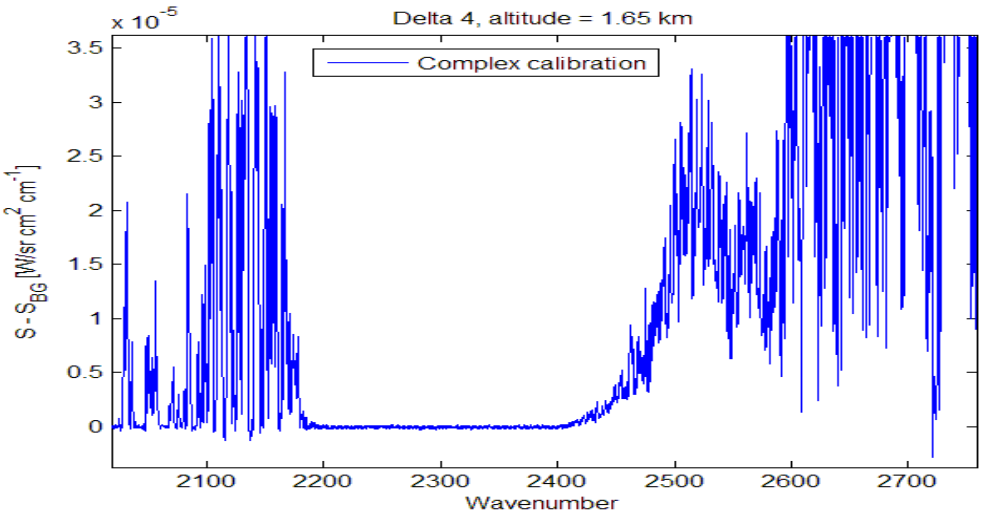

Figure 8: Plume spectrum, at an altitude of 1.65 km and a range of 59 km, at 1cm^{-1} resolution, after background subtraction, as evaluated by the complex calibration method (see Figure 3 for the result with the standard method)

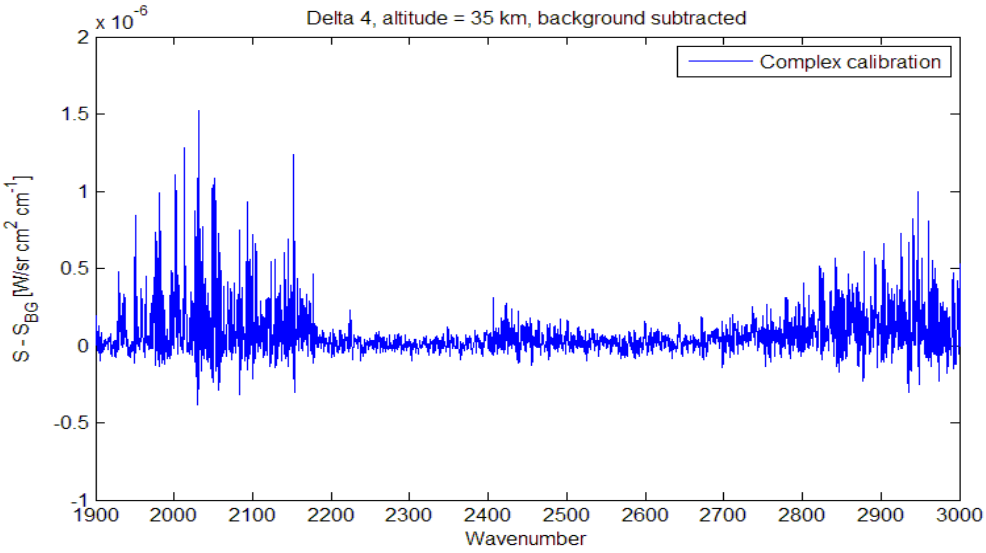

Figure 9: Plume spectrum (background subtracted) as calibrated with the complex calibration method (see Figure 5 for the result with the standard method)

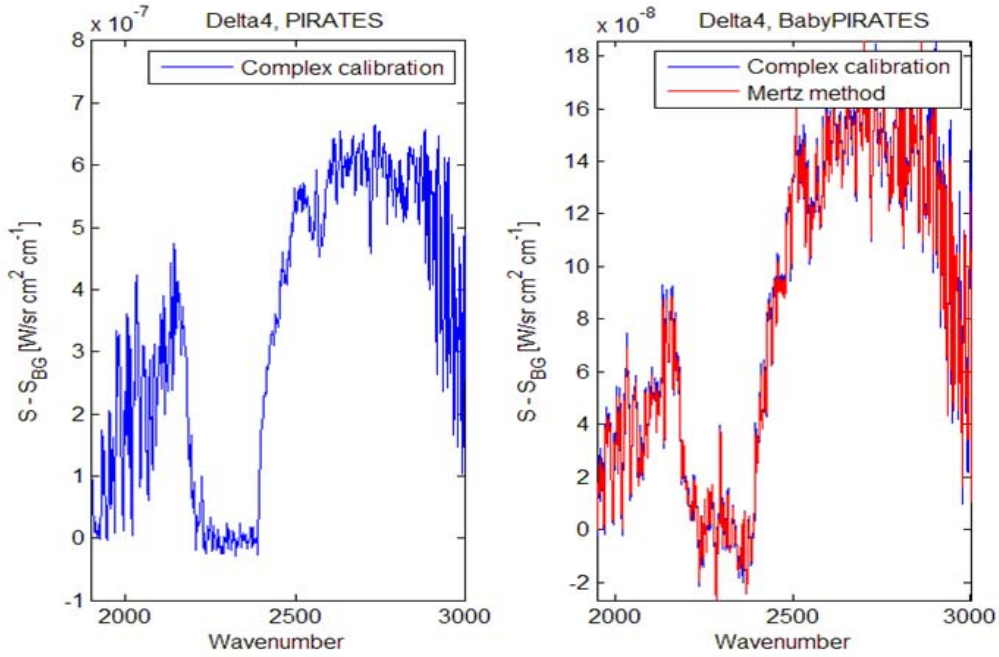

Figure 10: Nozzle spectrum, background subtracted, for DELTA-4 at an altitude of 122 km and a range of 216 km, at 4 cm^{-1} resolution . The left panel show the results obtained for PIRATES with the complex calibration method (see Figure 6 for the standard calibration result). In the right panel are shown the results obtained with BP for the complex and the standard calibration methods.

So far, it has been shown that most of the negative features present in the DELTA-4 data produced using the standard calibration method can be corrected for with the complex calibration method (these were all background subtracted spectra). The advantage of presenting background subtracted results is that any systematic errors in the evaluation of the offset O_c will cancel out. A typical background spectrum obtained with the complex calibration method is shown by the red line in Figure 11. Strangely, this background appears to be negative. The shape of the spectrum without background subtraction may depend on the offset O_c, which is evaluated according to Eq. (15). Since the offset is directly related to the theoretical ambient BB expression, it depends on the ambient temperature T_a. The recorded ambient temperature in this example was 24°C, for both PIRATES and BP instruments. However, unlike BP, PIRATES had a heater inside the instrument, to prevent condensation, and this difference could have affected the ambient temperature. The background spectra obtained from the complex calibration method, for different values of T_a, are shown in Figure 11 . By using $T_a \approx 40$°C, the PIRATES background turns out to be comparable to that for BP, except in the CO_2 [2300-2400] cm^{-1} band. The signal intensity in this band reflects directly the local CO_2 emission; a higher ambient temperature would manifest itself by higher signal intensity in this CO_2 band, as seen in the plot. However, it has not been possible to fit the background of all pixel with an unique ambient temperature: the ambient temperatures needed to satisfy all pixels were covering the range $24\ ^{o}\text{C} < T_a < 50\ ^{o}\text{C}$. This peculiarity remains unexplained.

Three components of radiation contribute to the instrumental offset O_c [7]: the emission from the optical components of the input port, the radiation from the optical components of the detector port emitted toward the beam splitter, and the suspected volume emission within the beam splitter. The phases associated with these respective contributions are, relatively to an external source's phase, identical, different by π, and different by $\pi/2$. Accordingly, the instrumental offset for PIRATES at DELTA-4 would have been dominated by the second contribution.

The instrument offset is a complex distribution in the complex calibration approach, while it is real in the standard method. However, the responsivities are real in both approaches, and negligible changes (smaller than 1 %) were found between these evaluated from each methods. The responsivity is always defined by Eq. (7), however the input functions X, Y and Z are given by Eqs. (8) and (13), respectively, for the standard and the complex methods. The small changes between the responsivities indicate a negligible instrument offset imaginary part (corresponding to small beam splitter emission) and that the magnitude of this offset was smaller than the BB emissions. Thus, the responsivities evaluated from each method will always be consistent, providing that the beam splitter is well behaved and that each BB are adjusted to a temperature high enough to overcome any possible source of heat inside the instrument.

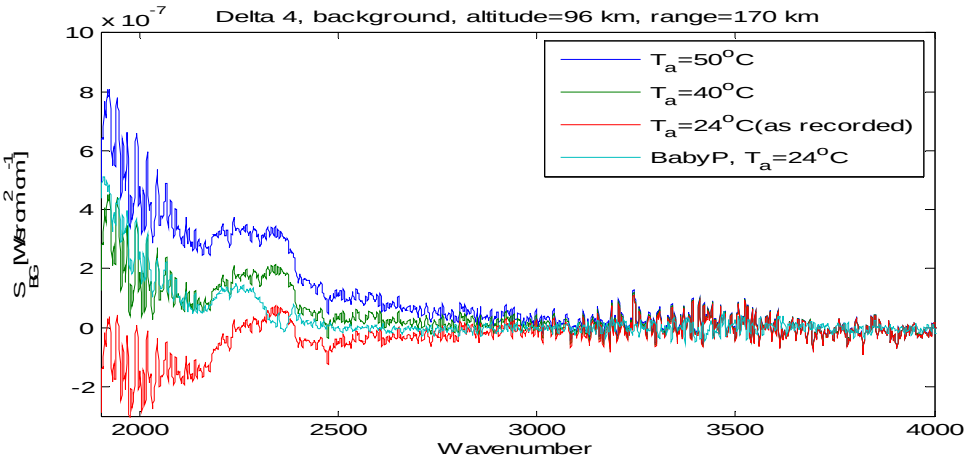

Figure 11:Effect of the ambient blackbody temperature on the background measurement, for PIRATES, during the DELTA-4 experiment. As a reference, the background measured by BP is also shown

5.2 Calibration from Background Subtracted Interferogram

A simple alternative approach to the complex method for producing a calibrated spectrum is to directly subtract the background's interferogram I_{BG} from the target interferogram I. This subtraction has to be done pixel by pixel, to avoid systematic errors between pixels. The complex background subtracted spectrum is thus given by

$$S_M - S_{M^{BG}} = FFT(I - I_{BG}) = R(S - S_{BG})e^{i(\phi+\phi_{ZPD})}, \tag{21}$$

where ϕ and ϕ_{ZPD} are respectively calculated from Eq. (14) and Eq. (20). The calibrated spectrum is simply given by

$$S - S_{BG} = \frac{(S_M - S_{M^{BG}})}{R} e^{-i\phi} e^{-i\phi_{ZPD}}. \tag{22}$$

The Revercomb method and the background subtracted interferograms method are mathematically identical. The advantage of the second approach is that the instrument offset does not have to be calculated as it has been cancelled out in the interferogram subtraction. This can be an important issue when there is a limited room for storage information. However, this method necessitates the knowledge of the corresponding background interferogram before each measurement. Alternatively, one could rather subtract the target and ambient blackbody interferograms, providing that there is no relative ZPD shift (i.e. if $\phi_{ZPD} = 0$). This would lead to S-S_a. Thereafter, one could simply add the theoretical ambient spectrum (with an atmospheric transmission function to take into account the absorption within the instrument) in order to isolate the calibrated spectrum S (target plus background spectrum).

5.3 Conditions under which the complex calibration method or the background subtracted interferogram method must be applied

We have shown that the complex calibration method and the background interferogram subtraction method, can remove some of the negative features in a spectrum generated using conventional treatment. It has been observed, however, that occasionally, as in Figure 3, that the negative features can also be removed from a Mertz method by using a higher number of points *M*. From the complex calibration method (CCM), a transformed complex spectrum, after background subtraction, is given as

$$S_M - S_{M^{BG}} = R(S - S_{BG})e^{i\phi}, \tag{23}$$

In this section, the relative phase ϕ_{ZPD} is simply ignored to highlight the differences between the Mertz and the complex calibration methods. By multiplying by $e^{-i\phi}$, the signal becomes (neglecting the residual noise for simplicity, in order to illustrate the problem)

$$S_{CCM} = \frac{\left|S_M - S_{M^{BG}}\right|}{R} = S - S_{BG} \tag{24}$$

In the standard method (Mertz), the background subtracted spectrum would be

$$S_{Mertz} = \frac{S_{pc} - S_{pc^{BG}}}{R} = \frac{R(S + O_c)e^{i\phi}e^{-i\phi_T} - R(S_{BG} + O_c)e^{i\phi}e^{-i\phi_{BG}}}{R} \tag{25}$$

where ϕ_T and ϕ_{BG} represent, respectively, the apparent target and background phases extracted by the Mertz method. Those apparent phases depend on the number of points *M* used for the low resolution interferogram. Different scenarios can be considered.

1. $\boldsymbol{S_{BG} << S}$ **and** $\boldsymbol{|O_c| << S}$**.** In that situation, we have $\phi_T = \phi$, such that :

$$S_{Mertz} \approx S \approx S_{CCM}\ . \tag{26}$$

2. $\mathbf{Re}(\boldsymbol{O_c}) > -\boldsymbol{S_{BG}}$**,** $\mathbf{Re}(\boldsymbol{O_c}) > -\boldsymbol{S}$ **and** $|\mathbf{Im}(\boldsymbol{O_c})| << |\mathbf{Re}(\boldsymbol{O_c})|$. Then we get $\phi_T = \phi_{BG} = \phi$, such that

$$S_{Mertz} = S - S_{BG} = S_{CCM} . \quad (27)$$

3. ***Re(O$_c$) < - S$_{BG}$, Re(O$_c$) > -S*** and ***|Im(O$_c$)|<< |Re(O$_c$)|.***

We would get $\phi_T = \phi$, and $\phi_{BG} = \phi + \pi$, so that

$$S_{Mertz} = S + O_c + (S_{BG} + O_c) = S + (S_{BG} + 2O_c) . \quad (28)$$

For $S < -(S_{BG} + 2O_c)$, we would obtain $S_{Mertz} < 0$, whatever the number of points M. This would give the impression that the signal is weaker than the background, as seen in the left panel of Figure 6. Now, if $S >> -(S_{BG} + 2O_c)$ everywhere, excepted in the strong atmospheric absorption bands, we would obtain

$$S_{Mertz} \approx S \approx S_{CCM} , \qquad \text{for } S >> S_{BG} + 2|O_c| \quad (29)$$

Inside the atmospheric absorption bands, for which $S=S_{BG}$, we should have $\phi_T = \phi_{BG} = \phi + \pi$, providing the number of points M is high enough to correctly describe the phase change between the high intensity regions and the absorption band regions. Otherwise, for small M, ϕ_T and ϕ_{BG} will be different at the edges of the absorption band regions, as seen in Figure 4. Then, we obtain

$$S_{Mertz} = 0 = S_{CCM} , \qquad \text{for } \sigma \text{ inside the atmospheric absorption band with } M \text{ large} \quad (30)$$

and

$$S_{Mertz} = (S_{BG} + O_c) e^{i\phi} (e^{-i\phi_T} - e^{-i\phi_{BG}}) , \text{ for } \sigma \text{ inside the band with } M \text{ small} \quad (31)$$

4. All other scenarios for which $|Im(O_c)|$ is non-negligible in front of S, would give $\phi_T \neq \phi$, and thus, different results for the Mertz approach than for the complex calibration method.

To summarize, the standard (Mertz) approach can be applied:

- when the offset is real and positive;
- or when the offset is real and negative, but smaller in magnitude than the background and the signal;
- or when the offset is negative and/or complex, provided that the target intensity is much larger than the offset and background. In this case, a large value for M must be used in order to handle correctly the points located near the strong atmospheric absorption bands.

As seen in Figure 3, a typical value for M would be 10% of N (N is the length of the interferogram), and rounded to the closest power of two.

The complex calibration method, or the background subtracted interferogram method, must be applied when none of these conditions are fulfilled.

At this point, the standard approach to process raw interferogram has been described, and a problem that can arise from that method has been discussed. Indeed, in the standard approach, an important instrument self-emission can make the spectrum look negative (after background subtraction). In this chapter, two approaches have been proposed to limit this feature, in order to allow a more accurate exploitation of the long range missile data. These two approaches can also be applied to any kind of measurements taken with PIRATES and BP.

In the next chapter, the source instabilities are discussed. It will be shown that these perturbations can also lead to negative features which cannot, however, be removed by the two calibration methods that have been proposed in this chapter. Some solutions will be suggested to reduce the importance of these features.

6 Source Noise

We have seen in the previous chapter that some negative features in the spectra could not be totally removed with a complex calibration method (Figure 9, for example). We show in this chapter that the origin of these remaining negatives peaks is most likely due to be source noise and we indicate how the source noise manifest itself in the data. Possible solutions to reduce these effects will also be discussed.

Under ideal conditions, the signal intensity $S_{pc}(\sigma)$ reaching the detector is constant over time. The intensity coming out of the modulator and detected at a position x is thus:

$$I(x) = c \int_{\sigma_{\min}}^{\sigma_{\max}} d\sigma S_{pc}(\sigma)\left[1 + \cos\left(2\pi\sigma x + \phi(\sigma)\right)\right] \tag{32}$$

where c is a constant and $\phi(\sigma)$ is the phase, due to beam splitter characteristics or signal delays, and causes asymmetry in the double-sided interferogram around the position x=0. The signal S_{pc} includes the effects of the detector responsivity and the instrument self-emission. For a time (position)-dependent signal, we rather have

$$I(x) = c \int_{\sigma_{\min}}^{\sigma_{\max}} d\sigma S_{pc}(\sigma)\left(1 + g(\sigma, x)\right)\left[1 + \cos\left(2\pi\sigma x + \phi(\sigma)\right)\right] \tag{33}$$

where the function $g(\sigma,x)$ tells by how much the intensity of each wavenumber fluctuates at position x. The AC interferogram is obtained by subtracting the DC component:

$$I_{AC}(x) = I(x) - \left\langle I(x) \right\rangle \tag{34}$$

After a Fourier transform, the complex-uncalibrated spectrum is obtained from:

$$
\begin{aligned}
S_M(\sigma_0) = \int_{-L}^{L} dx I_{AC}(x) e^{-i2\pi\sigma_0 x} &= c\int_{-L}^{L} dx \int_{\sigma_{\min}}^{\sigma_{\max}} d\sigma S_{pc}(\sigma)\cos\big(2\pi\sigma x + \phi(\sigma)\big)e^{-i2\pi\sigma_0 x} \\
&\quad - \frac{\sin(2\pi\sigma_0 L)}{\pi\sigma_0}\left[\big\langle I(x)\big\rangle - c\int_{\sigma_{\min}}^{\sigma_{\max}} d\sigma S_{pc}(\sigma)\right] \\
&\quad + c\int_{\sigma_{\min}}^{\sigma_{\max}} d\sigma S_{pc}(\sigma)\int_{-L}^{L} dx g(\sigma,x) e^{-i2\pi\sigma_0 x} \\
&\quad + c\int_{-L}^{L} dx \int_{\sigma_{\min}}^{\sigma_{\max}} d\sigma S_{pc}(\sigma) g(\sigma,x)\cos\big(2\pi\sigma x + \phi(\sigma)\big)e^{-i2\pi\sigma_0 x}.
\end{aligned}
\tag{35}
$$

The first term of this equation represents the spectrum without time perturbations. The second term represents a sinc function centered at $\sigma_0 = 0$, with a coefficient dependent on the averaged modulated signal and the total radiation in the band $[\sigma_{\min}, \sigma_{\max}]$. The third term corresponds to the product of the frequency distribution with the Fourier transform of the fluctuations, and finally summed over all frequencies. The effect of this term is visible at low frequencies, as shown in Figure 12. This region of frequencies, located well below the lower detection limit of the detectors, corresponds to the fluctuations frequencies. Finally, the last term from Eq. (35) represents the effect of source fluctuations within the detection limits. The effect of this last term is studied in Figure 13 and Figure 14. To highlight the effect of source noise, the phase $\phi(\sigma)$ has been set to zero in Eq. (35). In Figure 13 (top-left panel), a theoretical spectrum *S1* is shown. This spectrum is obtained by taking the FFT of an interferogram *I1* having *N* points. This spectrum corresponds to the first term of Eq. (35), with $L = N\Delta x/2$. On the top-right panel, the low-resolution spectrum *S2* is obtained by truncating the initial interferogram down to *M* points ($M = 8192$ and $N = 32768$). The interferogram *I2* is zeropadded so that its length is *N* points. On the bottom-left panel, the spectrum is obtained from the FFT of the sections of the interferogram not used in the top-right panel. This corresponds to defining an interferogram *I3* by *I3=I1*, followed by *I3*[*-M/2, M/2*] =0. At this point, the spectra are connected by *S1=S2+S3*. Finally, on the last panel of Figure 13, the effect of the last term of Eq. (35) is evaluated. For this example, the fluctuation is taken to be

$$
g(\sigma,x) = (f-1)\left[\Theta\left(-\frac{M}{2}\Delta x - x\right) + \Theta\left(x - \frac{M}{2}\Delta x\right)\right], \tag{36}
$$

where *f* represents the factor by which the edges of the unperturbed interferogram are weighted, to become the perturbed interferogram (for no fluctuations: *f*=1). The bottom-right panel of Figure 13 shows the sum of the first and last terms of Eq. (35), with *f*=2. In other words, this means that the edges of the interferograms (the sections [*-N/2, -M/2*] and [*M/2, N*/2]) are weighted by a factor 2 before doing the FFT. The effect of different weighting factors *f* on the complex-uncalibrated signal from Eq. (35) is displayed in Figure 14. For *f>1*, all extremities of the spectrum are stretched. The negative peaks thus correspond to stretched absorption lines. On the

other side, for *f<1*, the spectrum appears compressed. The *f*<1 case shows similar effect than a strong apodization or truncation operation in an unperturbed interferogram.

As it uses only a small section around the interferogram ZPD to evaluate the phase, the Mertz approach is useless to correct those negative peaks. The same conclusion appears for the complex calibration approach, since the fluctuations are random, changing from scan to scan; there is no information about the fluctuations in the blackbody phases. However, the spectral resolution affects the strength of the negative peaks, as seen in Figure 15. The spectrum (1 cm^{-1} resolution) from Figure 5 is shown and compared with the spectrum obtained by truncating the corresponding interferogram to a 4 cm^{-1} resolution. Limiting the maximal path difference, and so decreasing the time needed for a scan, reduce the probability to have large intensity variations between the different sections of the interferogram. Indeed, we observe in Figure 15 that almost all negative peaks have disappeared. The same effect, although less accentuated, is seen by using stronger apodization function. The Hamming apodization, in Figure 16, can also be used to reduce the importance of negative peaks.

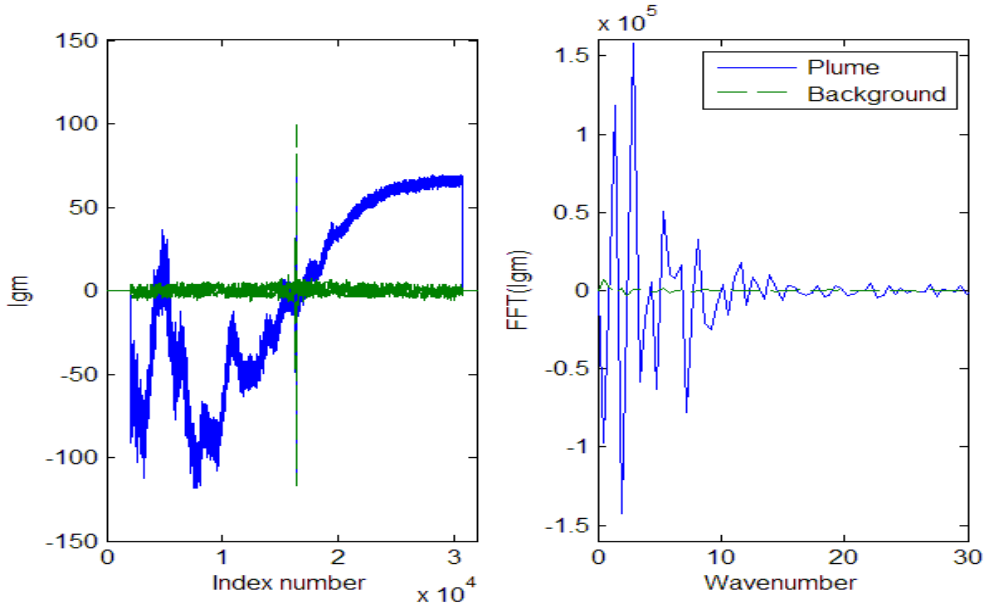

Figure 12: Typical interferograms for plume and background distributions (left panel), and the results after the FFT (right panel). The larges fluctuations in the plume's interferogram result in large peaks in the spectrum, at low frequency.

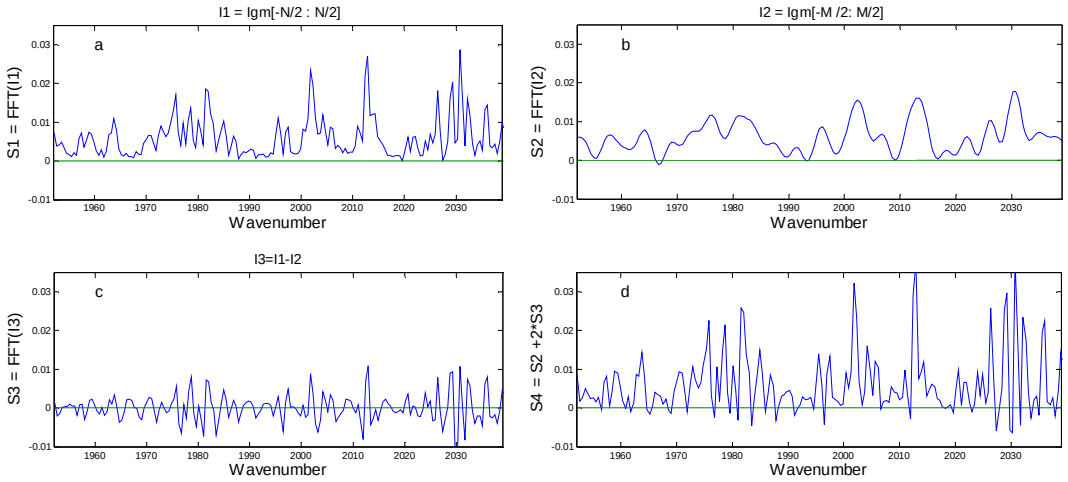

Figure 13: Effect of source fluctuation on a theoretical spectrum. a) Spectrum obtained from the full interferogram; b) low-resolution spectrum obtained from a small interferogram's section around the ZPD; c) spectrum obtained from the interferogram's sections not used in part b; d) spectrum obtained by the full interferogram weighted in the edges (part c) by a factor of 2, hence introducing negative features in the spectrum. For this example, N=32768 and M=8192.

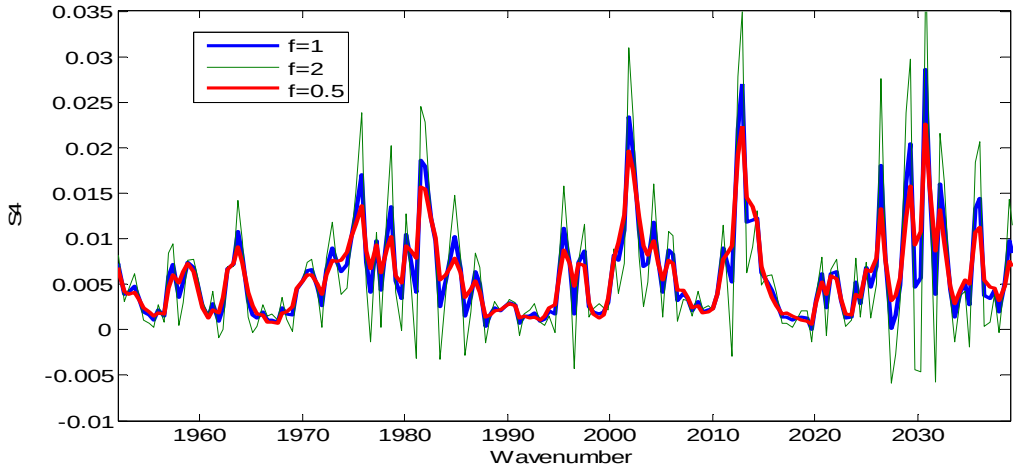

Figure 14: Effect of the weighing factor f on a theoretical spectrum. The green line corresponds to the spectrum of Figure 13 (panel d), with f=2, while the blue line corresponds to the unperturbed spectrum, Figure 13 (panel a). The red line (f=0.5) shows similar effect to what would produced a stronger apodization.

To see how the appearance of negative peaks evolves with time, the [2100-2200] cm^{-1} band is selected. The level of noise L_N is evaluated from the CO_2 band [2300-2400] cm^{-1} (that band

contains only noise since the background has been subtracted from the signal). The maximum intensity in the [2100-2200] cm^{-1} band is denoted by M_I, while the parameter r_N is defined by

$$r_N = \frac{\sum_{\sigma=2100}^{2200cm^{-1}} \left|S(\sigma) - S_{BG}(\sigma)\right| \Theta\left(S_{BG}(\sigma) - S(\sigma)\right)}{\sum_{\sigma=2100}^{2200cm^{-1}} \left|S(\sigma) - S_{BG}(\sigma)\right|}, \qquad \text{for } M_I > 10\, L_N$$

$$r_N = 0, \qquad \text{for } M_I \leq 10\, L_N. \tag{37}$$

The unit step function is defined by $\Theta(x)=1$ for $x \geq 0$, otherwise $\Theta(x)=0$. So, for $M_I > 10\, L_N$, the parameter r_N is defined by the integrated intensity of the negative signal, divided by the integrated intensity of the signal magnitude, in the [2100-2200] cm^{-1} band. The $M_I > 10\, L_N$ condition is introduced to get rid of the signals S-S_{BG} consisting of noise only (i.e. when $S \sim S_{BG}$). Without this condition, we would obtain $r_N \sim 0.5$, since the noise after phase correction oscillates randomly from negative to positive. For a given frame, the r_N parameter is evaluated for each pixel and the maximal value calculated among the pixels is displayed as a function of the frame number in Figure 17, for 1 cm^{-1} and 4 cm^{-1} resolution. The size of r_N, which represents the effect of source fluctuations, is again much smaller at low resolution, as previously seen in Figure 15.

Source noise can be generated by the fluctuations of the source's size and intensity, and also by tracking instabilities. The larger peaks displayed in Figure 17 have been related to tracker fluctuations. For example, as going from frame 42 to frame 43, the whole plume has moved one pixel to the right while the plume's shape has not change. Unlike for the DELTA-4 measurements, where the tracking was done manually, the tracking was automated for the ATLAS II data collection. In Figure 18, the time (frame number) evolution of the r_N parameter is shown for both DELTA-4 and ATLAS II data. While the average r_N value appears to be comparable for the two experiments, there are no huge peaks in ATLAS II, indicating that the tracking was more stable. The spatial distribution of the negative peaks is highlighted in Figure 19. The countour plot of the integrated intensity is shown for DELTA-4 (PIRATES), at four different ranges. The grids represent the 8x8 pixels arrays. The dashed lines represent the integrated intensity distributions, while the solid lines show the negative peaks distributions. It turns out that the negative peaks are mostly located on the edges of the plume, where the intensity is lower. This result is consistent with the hypothesis that the source noise is mostly caused by a relative displacement of the plume (relative to the instrument), rather than intensity fluctuations in the rest frame of the plume. Indeed, source noise is caused by fluctuation of the incoming radiation within a scan period. Since the central part of the plume covers in general more that one pixel (see Figure 19), that region would be less affected by the displacement of the tracker during one scan. However, for the regions at the edges of the plume, the effect of moving, during one scan, from a region with no plume to a region with plume at mid to high intensity, would be much more important. These peripheral regions of the plume also correspond to highly unstable zones (low density gas mixing with the air from the atmosphere).

The rapid movements of the tracker and the spatial instabilities of the plume have a direct impact on the measurement quality. At low resolution, these perturbations are minimized. When

scanning at high resolution, however, it is essential to track as smooth as possible. The intensity fluctuations in the rest frame of the plume (temperature drop for example) could certainly also produce negative peaks, although those observed in DELTA-4 are probably caused by a relative displacement of the plume. Assuming, for example, that the negative peaks observed in Figure 15 (at $1cm^{-1}$) are caused only by fluctuation in the emission of the plume, by comparing with the simple calculations shown in Figure 13, an approximate variation by a factor 2, in the edge of the interferogram, would be necessary to reproduce the strength of the negative peaks shown in Figure 15. This factor of 2, is nothing rigorous, but it gives an impression of how much the intensity need to fluctuate to generate the observed negative features.

We have seen in this chapter how the source noise can distort an interferogram and cause artifacts in a spectrum. The remaining negative features in the DELTA-4 measurements results, left by the complex calibration approach (see Figure 9), have certainly been caused by source noise. These negative features are mostly visible on spectra originating from the periphery of the plume, and these features can be reduced either by a smoother tracking, or by a strong apodization, or by scanning faster, or by selecting a lower spectral resolution. Finally, an alternative way to reduce the effect of source noise, in order to have better looking spectra, could be the degradation of the optical focus. Indeed, for a not optimized focus, an image does not produce a spot in a pixel, but rather a blur that can extend on the neighbouring pixels. That blur effect would of course reduce the spatial resolution of an object. However, it would also reduce the source noise coming from the sharp discontinuity between the background and the edge of the plume.

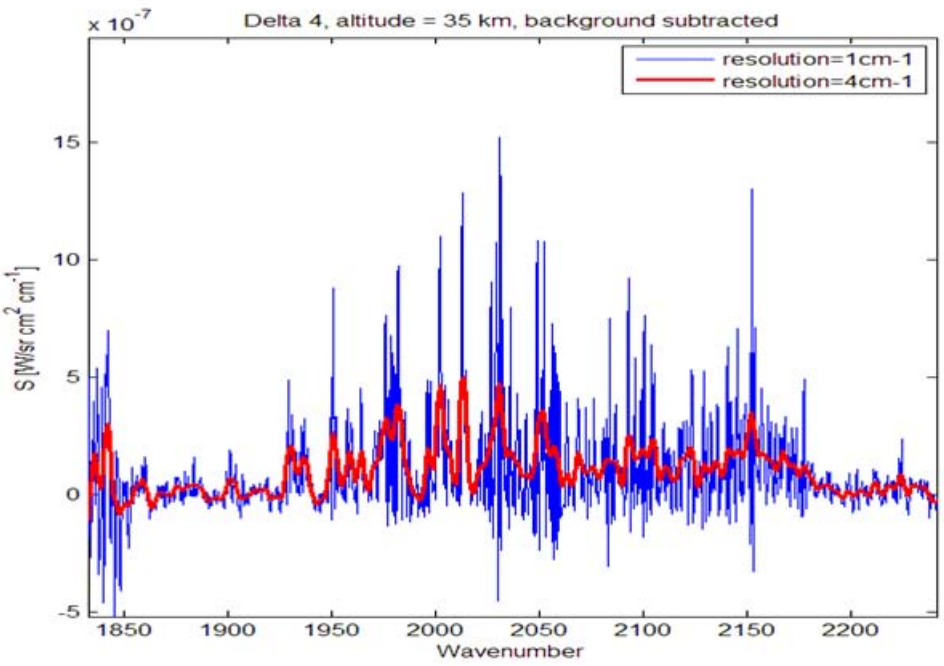

Figure 15: Effect of the resolution on the negative features after background subtraction

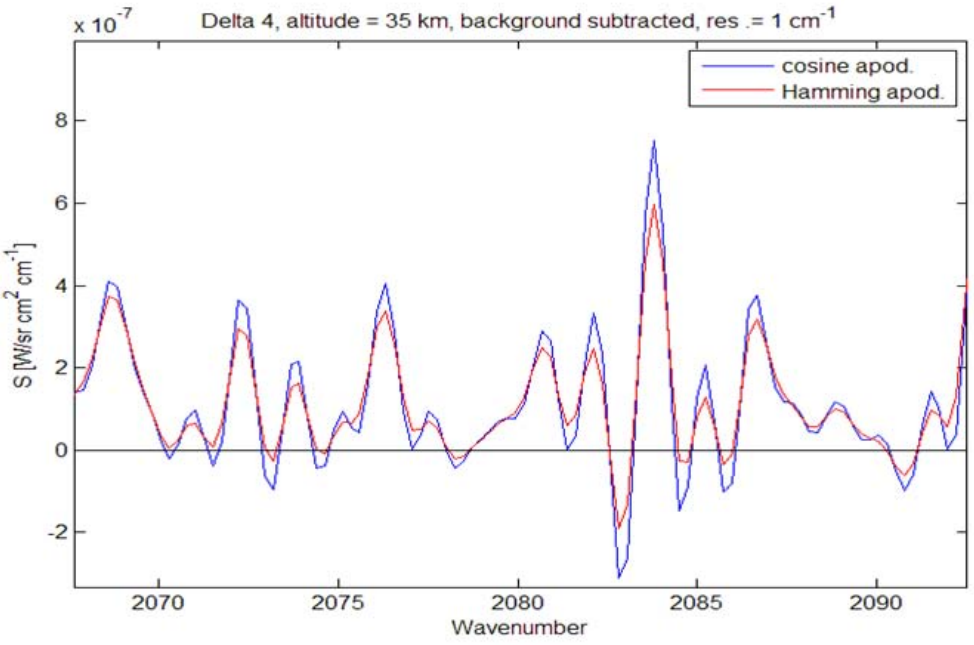

Figure 16 : Effect of apodization on negatives peaks

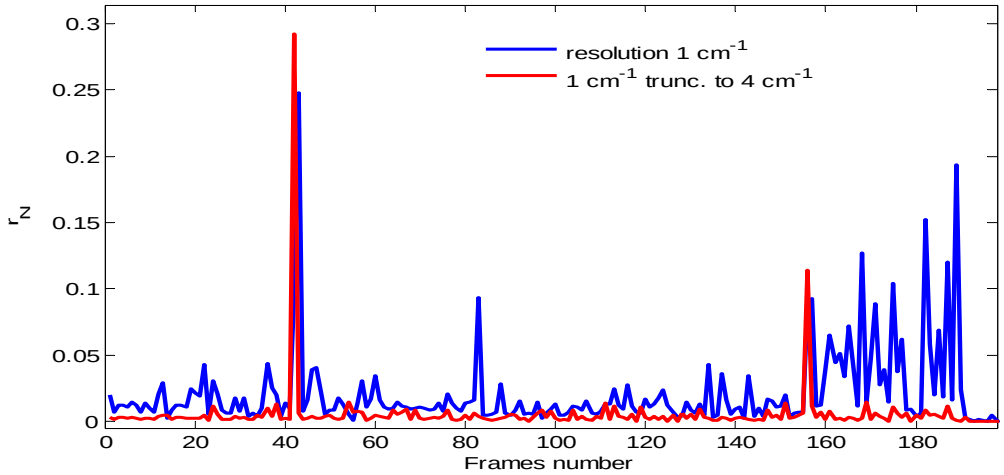

Figure 17: Time evolution of the negative peaks in DELTA4, with PIRATES, for 1 cm^{-1} and 4 cm^{-1} resolution. The r_N parameter represents the fraction of negative peaks in the band [2100-2200]cm-1. For a given frame number, the highest rN calculated among the pixel is shown. The x-axis indicates frames number, each frame corresponding to 0.23 second.

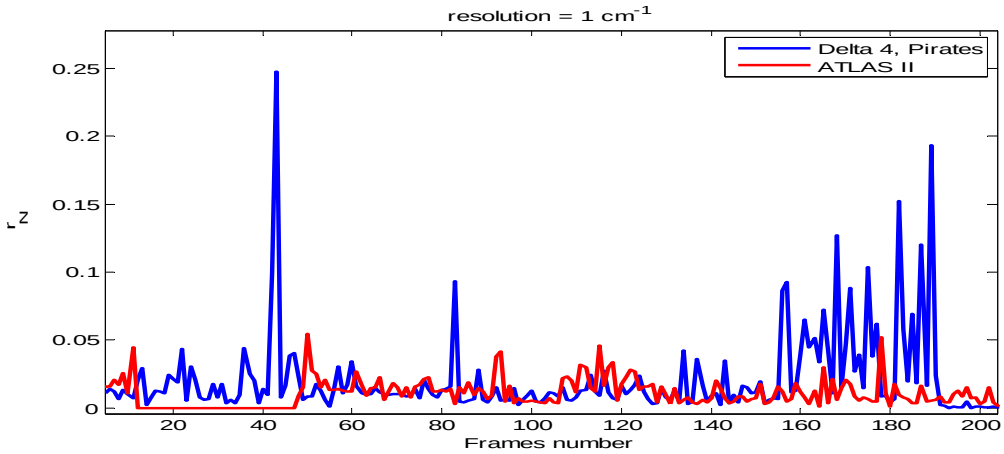

Figure 18: Time evolution of the negative peaks, at a resolution 1 cm^{-1}, for DELTA4 and Atlas II, with PIRATES. The r_N parameter represents the fraction of negative peaks in the band [2100-2200]cm^{-1}. For a given frame number, the highest r_N calculated among the pixel is shown. The x-axis indicates frames number, each frame corresponding to 0.23 second.

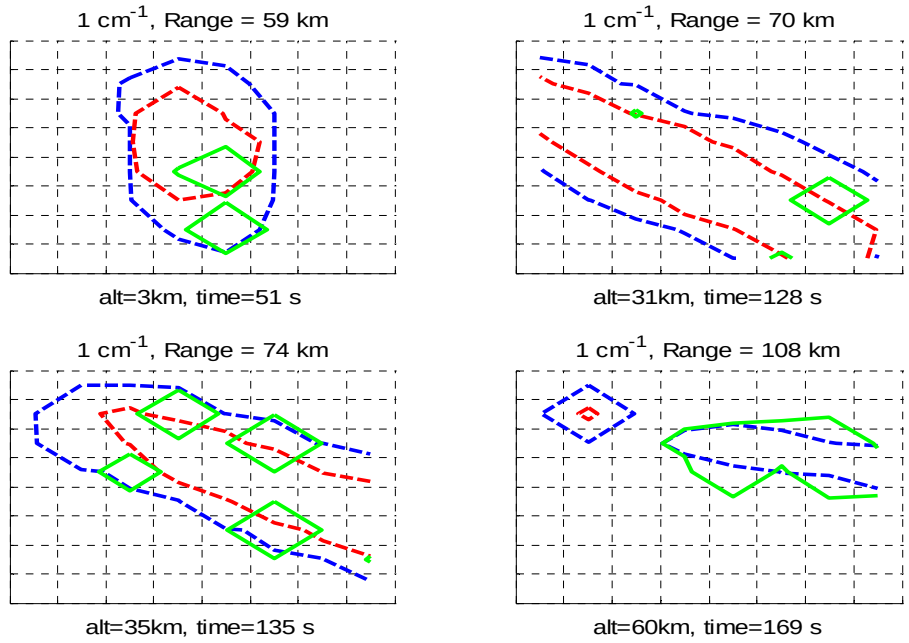

Figure 19: Countour plots in the 8x8 pixels array, for different altitudes, at 1 cm^{-1} resolution. The dashed lines show the spatial distribution of the energy in the plume. For each pixel, the energy is integrated in the [2000-45000] cm^{-1} band. The red lines delimit regions with ten times more energy than the blue line's. The solid green lines indicate regions with a r_N parameter larger than 0.001. At high altitude, the plume intensity is lower and the nozzle is not hidden anymore. The nozzle is apparent at an altitude of 60 km (on the top left corner of the array).

7 Conclusions

The PIRATES, BP and AIRIS systems are hyperspectral imagers (videos) that can enhance the Canadian Forces' Intelligence, Surveillance and Reconnaissance capabilities. These very flexible sensors have been optimized to allow quick modification of the time and spectral resolutions, with a fixed spatial resolution of 8x8 pixels.

The standard method to process the PIRATES and BP raw data (interferograms) into calibrated spectra has been discussed in this report. It has been shown how an important negative or complex instrument self-emission, and with a magnitude larger than that of the background, can produce negative target intensities, when the standard method is used. The instrument self-emission is negative when it is dominated by the detector port. Two algorithms have thus been proposed to eliminate this self-emission effect. The first proposed method relies on a twenty year old approach [6], in which the phases extracted from blackbody spectra, during the calibration step, are extracted and directly applied to the target spectra to be calibrated. However, it has been observed that the coadded and single scan interferograms can be not aligned. An algorithm has been developed to align the ZPD and make that method applicable. In a second proposed method, a background interferogram is subtracted to the target interferogram, before doing the phase correction and the calibration. The two proposed calibration methods corrected successfully the spectral negatives features caused by the thermal self-emission of the instrument. The first method generates a spectrum including target and background, while the second method generates directly the target spectra. When a background spectrum is subtracted from the first method's result, both methods turn out to be mathematically equivalent. The total target plus background spectrum could however be recouped in the second method, if the coadded and single scan ZPD are aligned correctly, by subtracting the ambient blackbody interferogram instead of the background interferogram. The total target plus background spectrum would finally be obtained by adding the theoretical ambient blackbody intensity distribution, in the spectral domain.

Signals from the sources that are not constant over time introduce source noise in the resulting spectra. This source noise can either stretch or compress the accentuated extremities of a spectrum, introducing in the former case, negative peaks that cannot be removed by the complex calibration method. It has been shown in this report that the main cause of source noise during missile signature measurements is likely to be the displacement of the source relatively to the instrument, rather than fluctuation of the local temperature of the source. The effect of source noise can be reduced either by scanning faster (the scan speed is however limited by the detectors responses), or by applying a strong apodization function (like Hamming), or by selecting a lower spectral resolution, or by degrading the optical focus, and finally, the most important, by tracking the plume as smoothly as possible.

To summarize, with the algorithms proposed for the calibration and the suggestions made to reduce source noise, more accurate information would be extracted from the current long range missile data and from future measurements.

References

[1] ARP 13mb: Real-time airborne IR-HIS for Improving Aerospace Surveillance Capabilities.

[2] J.W. Cooley and J. W. Tukey, "*An Algorithm for the Machine Computation of the Complex Fourier Series*", Mathematics of Computation, Vol. 19, April 1965, pp. 297-301.

[3] L. Mertz, "Auxiliary computation for Fourier spectrometry", *Infrared Phys.* **7**, 17 (1967).

[4] L. Mertz, *Transformations in Optics*, Wiley-Interscience, New York (1965).

[5] R. J. Bell, *Introductory Fourier Transform Spectroscopy*, Academic Press, New York, 1972.

[6] H. E. Revercomb, H. Buijs, H. B. Howell, D.D La Porte, W. L. Smith, and L. Sromovsky, "*Radiometric calibration of IR Fourier transform spectrometers: solution to a problem with the high-resolution interferometer sounder*", Appl. Opt. **27**, 3210 (1988).

[7] J. Schreiber, T. Blumenstock, and H. Fischer, "*Effects of the self-emission of an IR Fourier-transform spectrometer on measured absorption spectra*", Appl. Opt. **35**, 6203 (1996).

Annex A Four-point calibration

A.1 Derivation of the responsivity *R* and instrument self-emission *O*

Four measurements are needed for this calibration

$$\begin{aligned} S_a &= R(B_a + O) \\ S_h^{f_1} &= R(f_1 B_h + E_{f_1} + O) \\ S_h^{f_2} &= R(f_2 B_h + O) \\ S_h^{f_1 f_2} &= R\left(f_2\left[f_1 B_h + E_{f_1}\right] + O\right) \end{aligned} \tag{A.1}$$

The left hand side of the above relationships represent the phase corrected uncalibrated signals, while B_h and B_a represent the radiances of the hot and ambient blackbodies, respectively. The emission of the first filter is denoted by E_{f1}. For the second filter, being placed between the modulator and the detector, its emission does not have to be taken into account. Defining the following functions:

$$\begin{aligned} X &= S_h^{f_1} - S_a = R(f_1 B_h - B_a + E_{f_1}) \\ Y &= S_h^{f_2} - S_a = R(f_2 B_h - B_a) \\ Z &= S_h^{f_1 f_2} - S_a = R(f_1 f_2 B_h - B_a + f_2 E_{f_1}) \end{aligned} \tag{A.2}$$

The filters functions are thus given by

$$\begin{aligned} f_1 &= \frac{X}{RB_h} + \frac{(B_a - E_{f_1})}{B_h} \\ f_2 &= \frac{Y}{RB_h} + \frac{B_a}{B_h} \end{aligned} \tag{A.3}$$

Putting these results back into the definition of the *Z* function, we obtain

$$
\begin{aligned}
Z &= R\left[\left(\frac{X}{RB_h}+\frac{(B_a-E_{f_1})}{B_h}\right)\left(\frac{Y}{RB_h}+\frac{B_a}{B_h}\right)B_h - B_a + \left(\frac{Y}{RB_h}+\frac{B_a}{B_h}\right)E_{f_1}\right] \\
&= \frac{1}{B_h}\left[\frac{XY}{R} + XB_a + Y(B_a-E_{f_1}) + R(B_a-E_{f_1})B_a - RB_aB_h + YE_{f_1} + RB_aE_{f_1}\right] \\
&= \frac{1}{B_h}\left[\frac{XY}{R} + B_a(X+Y) + RB_a(B_a-B_h)\right]
\end{aligned}
\tag{A.4}
$$

Regrouping the terms, we obtain

$$
R^2\left(\frac{B_a}{B_h}(B_a-B_h)\right) + R\left(\frac{B_a}{B_h}(X+Y)-Z\right) + \frac{XY}{B_h} = 0 \tag{A.5}
$$

We thus have a quadratic relationship $aR^2+bR+c=0$, with $a < 0$ and $c > 0$. Since the responsivity has to be positive, the final expression is

$$
R = \frac{-\left(\frac{B_a}{B_h}(X+Y)-Z\right) - \sqrt{\left(\frac{B_a}{B_h}(X+Y)-Z\right)^2 - 4\frac{XY}{B_h}\left(\frac{B_a}{B_h}(B_a-B_h)\right)}}{2\left(\frac{B_a}{B_h}(B_a-B_h)\right)} \tag{A.6}
$$

The instrument offset is given by

$$
O = \frac{S_a}{R} - B_a \tag{A.7}
$$

It is interesting to note that neither the responsivity nor the offset expressions depend on the filter's emission E_{f1}.

A.2 Regions of strong CO2 or H2O absorption into which *R* and *O* are interpolated.

The strong CO_2 and H_2O absorption regions cause the responsivity R to be very close to zero. This behaviour can introduce large fluctuations into a calibrated spectrum, which is proportional to $1/R$. To avoid this, the instrument responsivity and offset are (linearly) interpolated over these

absorption regions. The calibrated results can be interpreted by the signals incident of the detector, rather that the signals incident on the telescope, since the effect of the column of air inside the instrument is not removed when we interpolate. The table below indicates the regions $\sigma_{min} < \sigma < \sigma_{max}$ into which we interpolate.

Table 1: Bands for the interpolation of the instrument responsivity and offset

σ_{min} [cm^{-1}]	σ_{max} [cm^{-1}]
1865.	1875.1
1875.1	1893.5
1893.5	1900.3
1900.3	1914.7
1914.7	1929.0
1929.0	1938.0
1938.0	1953.2
1953.2	1964.6
1964.6	1973.8
1986.0	1997.2
2014.2	2030.9
2037.5	2051.1
2059.1	2072.0
2085.1	2095.4
2111.0	2119.7
2133.8	2144.0
2159.2	2166.8
2284.0	2405.0
2948.0	3001.0
3001.0	3042.0
3042.0	3074.0
3074.0	3091.7
3091.7	3139.9
3205.6	3224.3
3224.3	3250.6
3250.6	3269.2
3269.2	3304.3
3304.3	3322.3
3322.3	3348.4
3348.4	3378.4
3378.4	3412.0
3412.0	3453.4
3453.4	3540.6
3540.6	3664.0

3664.0	3776.2
3776.2	3911.8
3911.8	4002.2
4002.2	4039.3
4039.3	4068.7
4068.7	4097.5
4097.5	4116.8
4126.3	4148.1

DOCUMENT CONTROL DATA

(Security classification of title, body of abstract and indexing annotation must be entered when the overall document is classified)

1. ORIGINATOR (The name and address of the organization preparing the document. Organizations for whom the document was prepared, e.g. Centre sponsoring a contractor's report, or tasking agency, are entered in section 8.)

Defence R&D Canada – Valcartier
2459 Pie-XI Blvd North
Quebec (Quebec)
G3J 1X5 Canada

2. SECURITY CLASSIFICATION (Overall security classification of the document including special warning terms if applicable.)

UNCLASSIFIED

3. TITLE (The complete document title as indicated on the title page. Its classification should be indicated by the appropriate abbreviation (S, C or U) in parentheses after the title.)

Effects of the instrument self-emission and source noise on long range infrared measurements of missile plumes

4. AUTHORS (last name, followed by initials – ranks, titles, etc. not to be used)

Turbide, S.; Smithson, T.; St-Germain, D.

5. DATE OF PUBLICATION (Month and year of publication of document.)

August 2009

6a. NO. OF PAGES (Total containing information, including Annexes, Appendices, etc.)

54

6b. NO. OF REFS (Total cited in document.)

7

7. DESCRIPTIVE NOTES (The category of the document, e.g. technical report, technical note or memorandum. If appropriate, enter the type of report, e.g. interim, progress, summary, annual or final. Give the inclusive dates when a specific reporting period is covered.)

Technical Report

8. SPONSORING ACTIVITY (The name of the department project office or laboratory sponsoring the research and development – include address.)

Defence R&D Canada – Valcartier
2459 Pie-XI Blvd North
Quebec (Quebec)
G3J 1X5 Canada

9a. PROJECT OR GRANT NO. (If appropriate, the applicable research and development project or grant number under which the document was written. Please specify whether project or grant.)

9b. CONTRACT NO. (If appropriate, the applicable number under which the document was written.)

10a. ORIGINATOR'S DOCUMENT NUMBER (The official document number by which the document is identified by the originating activity. This number must be unique to this document.)

DRDC Valcartier TR 2008-557

10b. OTHER DOCUMENT NO(s). (Any other numbers which may be assigned this document either by the originator or by the sponsor.)

Project Arrangement PA-CA-MDA-02-0001

11. DOCUMENT AVAILABILITY (Any limitations on further dissemination of the document, other than those imposed by security classification.)

UNLIMITED

12. DOCUMENT ANNOUNCEMENT (Any limitation to the bibliographic announcement of this document. This will normally correspond to the Document Availability (11). However, where further distribution (beyond the audience specified in (11) is possible, a wider announcement audience may be selected.))

UNLIMITED

13. ABSTRACT (A brief and factual summary of the document. It may also appear elsewhere in the body of the document itself. It is highly desirable that the abstract of classified documents be unclassified. Each paragraph of the abstract shall begin with an indication of the security classification of the information in the paragraph (unless the document itself is unclassified) represented as (S), (C), (R), or (U). It is not necessary to include here abstracts in both official languages unless the text is bilingual.)

The DRDC Valcartier Spectral Imagery Laboratory currently supports hyperspectral imagers designed for field measurements. The ground-based Passive Infrared Ranging And Target Evaluation System (PIRATES) has been used over the years for the infrared signature characterization of different kinds of military related targets. This report highlights some issues observed in recent long range missile IR detection results, such as large negative features in the calibrated spectra. The bulk of these negative features are found to be related to instrument self-emission. Two algorithms are proposed to eliminate these features. The remaining negative peaks were the result of source instability, and appear principally in the peripheral region of the missile plume. Solutions are proposed to limit these negative features, such as tracking the missiles as smoothly as possible. The algorithms and solutions proposed will allow for the extraction of more accurate information from the original data.

Le laboratoire d'imagerie spectrale de RDDC-Valcartier supporte présentement des imageurs hyperspectraux optimisés pour la mesure sur le terrain. Le capteur PIRATES a d'ailleurs été utilisé au fil des ans pour caractériser diverses cibles militaires à partir du sol. Ce rapport présente certaines anomalies observées dans les récentes mesures infrarouges de missiles à longue portée, notamment l'apparence de régions spectrales négatives. L'émission interne de l'instrument est responsable de la majorité des zones négatives. Deux algorithmes sont alors proposés pour éliminer ces effets indésirables. Les instabilités de source causent également l'apparence de raies négatives. Ces instabilités sont plus accentuées dans les régions périphériques du panache produit par les missiles. Des solutions sont proposées pour limiter l'impact de ces instabilités, dont la mise au point d'un système de poursuite aussi régulier que possible. Les algorithmes et solutions proposés dans ce rapport vont permettre une utilisation plus rigoureuse des mesures de missiles à longue portée, ainsi que de toute autre signature mesurée par le capteur.

14. KEYWORDS, DESCRIPTORS or IDENTIFIERS (Technically meaningful terms or short phrases that characterize a document and could be helpful in cataloguing the document. They should be selected so that no security classification is required. Identifiers, such as equipment model designation, trade name, military project code name, geographic location may also be included. If possible keywords should be selected from a published thesaurus, e.g. Thesaurus of Engineering and Scientific Terms (TEST) and that thesaurus identified. If it is not possible to select indexing terms which are Unclassified, the classification of each should be indicated as with the title.)

Infrared; spectral imagery; complex calibration; source noise

Defence R&D Canada

Canada's Leader in Defence
and National Security
Science and Technology

R & D pour la défense Canada

Chef de file au Canada en matière
de science et de technologie pour
la défense et la sécurité nationale

www.drdc-rddc.gc.ca